Research Square

Preprints are preliminary reports that have not undergone peer review.
They should not be considered conclusive, used to inform clinical practice,
or referenced by the media as validated information.

Autism-associated Shank3B deletion drives widespread dorsal cortical hyperactivity, amplified sensory responses and accelerated propagation

Allen Chan

awchan@ualberta.ca

University of Alberta

Zijia Yu

University of Alberta

Yonglie Ma

University of Alberta

Ryan Zahacy

University of Alberta

Ian Winship

University of Alberta

Article

Keywords:

Posted Date: August 22nd, 2026

DOI: https://doi.org/10.21203/rs.3.rs-10732790/v1

License: This work is licensed under a Creative Commons Attribution 4.0 International License.
Read Full License

Additional Declarations: No competing interests reported.

Abstract

Altered sensory processing is common in autism, but how disruption of autism-risk genes alters the cortex-wide dynamics underlying sensory responses remains unclear. Using wide-field mesoscale calcium imaging, we mapped spontaneous and sensory-evoked activity across dorsal cortex in Shank3B$^{-/-}$ mice, a model of disruption of the high-confidence autism-risk gene SHANK3, which encodes a postsynaptic scaffolding protein. Compared with controls, Shank3B$^{-/-}$ mice showed stronger cortical responses to visual and whisker stimulation, greater variability in spontaneous activity and sensory responses across trials, and faster spread of evoked activity across the cortex, while the direction of spread remained preserved. More broadly, spontaneous activity was elevated across most imaged regions, revealing a widespread hyperactive cortical state rather than an isolated sensory-circuit abnormality. Within this distributed phenotype, barrel and secondary somatosensory cortices showed the most informative resting-state signatures of genotype. These findings establish an in vivo systems-level link between disruption of a high-confidence autism-risk gene and a distributed hyperactive cortical state that amplifies, destabilizes, and accelerates sensory responses, providing a circuit-level framework for understanding sensory hyper-responsivity in autism.

Introduction

Autism spectrum disorder (ASD) is a complex neurodevelopmental condition that affects how individuals perceive and interact with the world. According to Diagnostic and Statistical Manual of Mental Disorders, Fifth Edition (DSM-5), core diagnostic criteria include deficits in social communication, repetitive behaviors, and restricted interests (1). Importantly, over 70% of children with ASD exhibit sensory processing abnormalities, now recognized as part of the official diagnostic framework (2). Moreover, ASD shows a strong male bias in prevalence (approximately 4:1 male:female), and increasing evidence indicates sex-specific differences in neural circuit function and sensory processing (3, 4).

Compared with typically developing peers, individuals with ASD score higher on all subscales of the Sensory Profile 2 including tactile, auditory, visual, and more, manifesting as under-responsiveness, over-responsivity, and sensation-seeking behaviors (5, 6, 7, 8). An electroencephalogram (EEG) study further links this hypersensitivity to cortical hyperexcitability, showing that ASD participants produce progressively larger spectral-power responses as stimulus contrast increases (9). Moreover, higher sensory scores predict more severe repetitive behaviors in children (8), while in adults greater hypersensitivity correlates with increased social touch avoidance and elevated autistic traits (10). Importantly, several studies report that males and females with ASD can differ in the severity or pattern of sensory symptoms and associated behaviors (11, 12). Taken together, these findings indicate that sensory processing abnormalities in ASD extend beyond perceptual differences to shape broader behavioral phenotypes, with potential sex-dependent nuances. Thus, elucidating how somatosensory cortex function is altered across different modalities, and understanding its underlying neurophysiological mechanisms, is essential for developing targeted interventions. Notably, resting-state brain activity metrics like root-mean-square(RMS) power are increasingly studied in ASD via EEG/

functional magnetic resonance imaging (fMRI), providing a translational framework for our approach. Genetic factors play a significant role in ASD, with synaptic plasticity-related genes accounting for much of the heritable risk. In particular, mutations in SHANK3, a postsynaptic scaffolding protein critical for synapse formation, are strongly linked to ASD (13, 14). Shank3B$^{-/-}$ mice exhibit core autism-like behaviors including impaired social interaction, increased repetitive grooming, altered communication, and synaptic deficits such as reduced spine density, disrupted glutamate receptor signaling, making them a well-validated preclinical model for circuit-level investigations of ASD (15, 16). Notably, more recent work has begun to uncover sex-specific differences in both behavioral phenotypes and cortical activity patterns in Shank3B and other ASD mouse models (17, 18), highlighting the need to examine male and female animals separately.

To quantify how Shank3 loss alters cortical network dynamics, we used mesoscale calcium imaging, which reports population $\Delta F/F_0$ over the dorsal cortex with subsecond sampling and mesoscopic spatial resolution, and has been applied to identify spontaneous cortical readouts in ASD mouse models (19, 20). This modality sits between cellular two-photon imaging and whole-brain fMRI, allowing simultaneous readout of local columns and inter-areal activity. In addition to amplitude-based features (peak $\Delta F/F_0$, area-above-threshold, onset latency), we extract optical-flow-derived propagation speed (mm/s; see Methods) to capture how activity spreads across cortex. Together, these measures let us assess resting and stimulus-evoked spatiotemporal patterns across multiple cortical areas.

In this study, we recorded GCaMP8s signals from anesthetized, head-fixed Shank3B$^{+/+}$ and Shank3B$^{-/-}$ mice of both sexes during brief visual and whisker stimulation, as well as during spontaneous resting activity. We (1) quantified sensory-evoked spatiotemporal features under anesthesia, (2) ranked these features via predictive modeling, (3) measured resting-state activity to validate the top predictors, and (4) confirmed that those predictors reliably classify Shank3B$^{-/-}$ vs. Shank3B$^{+/+}$ in both sensory and resting contexts. Details are provided in the Methods section.

Materials and methods

Animals

All procedures were approved by the University of Alberta Health Sciences Laboratory Animal Services and complied with Canadian Council for Animal Care guidelines. We used 2– to 6–month–old B6.129-Shank3tm2Gfng/J mice (JAX stock #017688), including both males and females, housed on a 12-h light/dark cycle in a temperature-controlled room. Breeding was established using multiple crossing strategies to obtain Shank3B$^{+/+}$, Shank3B$^{+/-}$, and Shank3B$^{-/-}$ offspring. Initially, we maintained Shank3B$^{+/-}$ x Shank3B$^{+/-}$ pairings. To supplement colony production, we also performed Shank3B$^{+/+}$ x Shank3B$^{+/+}$, Shank3B$^{-/-}$ x Shank3B$^{-/-}$, Shank3B$^{+/-}$ x Shank3B$^{+/+}$, and Shank3B$^{+/-}$ x Shank3B$^{-/-}$ pairings. All experimental animals were derived from these crosses. Pups were genotyped by standard PCR before any surgical or imaging procedures, and whenever possible, littermates of different genotypes

were co-housed. Mice had ad libitum access to food and water and were monitored daily for health and well-being. All analyses pooled both sexes except for Figs. 2 and 3, which included male mice only (n = 5 ~ 6 per genotype). Among the pooled-sex analyses, sample sizes were n = 9 ~ 11 per genotype for the sensory-evoked and propagation measures (Figs. 4 and 5) and n = 13 per genotype for spontaneous activity (Fig. 6); the larger sample size for spontaneous activity reflects additional animals that were retained for this measure but excluded from the evoked-response analyses because sensory stimulation was unsuccessful.

Chronic cranial window implantation

Mice were anesthetized with 4% isoflurane and maintained on 2% isoflurane in pure oxygen throughout the surgery. Ophthalmic gel was applied to protect the eyes from desiccation, and body temperature was kept at 37°C via an electric heating pad with feedback thermistor. After subcutaneous injection of 0.25% bupivacaine at the planned incision site, the scalp was retracted to expose the dorsal skull. The exposed surface was cleaned with sterile saline, dried, and then covered with transparent dental cement (C&B-Metabond, Parkell Inc.) onto which a 10 x 10 mm glass coverslip was placed to create a chronic transcranial window (as described in reference 35).

A stainless-steel head bar was positioned over the posterior cortex on top of the fresh cement and further secured by additional dental cement. At the conclusion of surgery, mice received a subcutaneous injection of buprenorphine (0.1 mg/kg) for analgesia and were allowed to recover in a cage with a warming pad until ambulatory. Animals were then returned to their home cages and monitored daily for at least 5 days before any imaging experiments.

Viral injection

Mice were initially anesthetized with 4% isoflurane and maintained on 2% isoflurane in pure oxygen for the duration of the procedure. A total volume of 45–50 µL of sterile saline containing 1 x 10^11 viral genomes of AAV-PHP.eB carrying the AAV-Syn-jGCaMP8s-AAV2/PHP.eB construct was injected into the retro-orbital sinus using a 30-gauge needle (36). This vector, produced by the Canadian Neurophotonics Platform Viral Vector Core Facility (RRID:SCR_016477), drives pan-neuronal expression of the jGCaMP8s calcium indicator under the synapsin promoter. After injection, mice were returned to their home cages and monitored until fully recovered. Four to five weeks later, animals exhibiting robust GCaMP8s fluorescence (confirmed via preliminary epifluorescence imaging) underwent mesoscale calcium imaging (Fig. 1A).

Imaging acquisition

Wide-field calcium imaging targeted a ~ 1 cm x 1 cm region of dorsal cortex through the chronic transcranial window. During imaging, two 470 nm blue LEDs (ThorLabs M470L2-C2) - one positioned

over each hemisphere - provided excitation light filtered through ThorLabs FBH470-10 (470 ± 10 nm). Emitted green fluorescence from GCaMP8s passed through a Semrock BrightLine FF01-525/30 – 25 emission filter mounted directly in front of the camera lens. Both excitation LEDs were adjusted so that cortical pixel intensities (gray values) remained between ~ 1000 and 3000 under imaging conditions. The room was kept dark except for a dim red safety lamp, and a blackout curtain enclosed the setup to eliminate ambient light. Imaging was captured at 12-bit resolution and 10 Hz using a Teledyne DALSA 1M60 CCD camera coupled to an EPIX EL1 frame grabber (XCAP 3.8 software).

Recordings of spontaneous and sensory-evoked activity

Recordings of spontaneous and sensory-evoked activity were performed under light isoflurane anesthesia. Mice were induced with 2–2.5% isoflurane and then maintained at 1.25% isoflurane in pure oxygen; after anesthesia stabilized for 3–5 minutes, each animal was head-fixed via the implanted head bar and placed in a dark, fully enclosed chamber illuminated only by a dim red safety lamp. Before any imaging, a reference photograph of the cortical surface was acquired without the emission filter to document window placement. Spontaneous calcium activity was then recorded at 10 Hz for 15 minutes with no external stimulation. Sensory-evoked activity was subsequently recorded, also at 10 Hz, in 8 or 200s trials (20–60 trials per stimulus intensity). All stimuli targeted the right side: for whisker stimulation, a single right-side whisker was deflected by a piezoelectric actuator at 3 s into each trial using 5 ms pulses at 20 Hz with 50 ms between pulses, for a total stimulation window of 500 ms; for visual stimulation, a single 50 ms flash from a blue LED (Rebel LED SinkPAD-II, Luxeon Star) was directed at the right eye from approximately 10 cm distance, again at 3 s into each trial. Consecutive trials were separated by a 7 s intertrial interval; no randomization or blank trials were included. Stimulus timing was controlled and synchronized by a Cambridge Electronic Design 1401 mk2 output board running Spike2 (v6.18), which sent TTL pulses to an AM Systems Model 2100 Isolated Pulse Stimulator (for piezo actuator control) and to the XCAP imaging software for frame alignment.

Optical-flow quantification

Widefield $\Delta F/F_0$ image stacks were sampled at 10 Hz (80 or 200 frames per trial; 128 × 128 pixels). To stabilize the flow estimates, spatial Gaussian smoothing ($\sigma = 4$ px) was applied before optical-flow computation within a dorsal-cortex mask. We estimated frame-to-frame propagation using the combined local–global (CLG) optical flow (toolbox of Afrashteh et al., 2017; parameter definitions per Jara-Wilde et al., 2015). Parameters were alpha = 0.030, ratio = 0.50, minWidth = 32, nOuterFPIterations = 7, nInnerFPIterations = 1, nSORIterations = 30. Speed was computed as $\|(u,v)\|$ in px/frame and converted to mm/s using our FOV and frame rate. Please see (21) for more details.

For each trial, instantaneous speed fields were averaged over pixels within the dorsal-cortex mask from stimulus onset to the peak of the $\Delta F/F_0$ response, yielding one speed value (mm/s) per trial. Trial values were then averaged within each animal to obtain one animal-level mean for visual and one for whisker stimulation. Flow direction was referenced to an anatomical frame with 0° medial (toward the midline),

90° anterior, 180° lateral, and 270° posterior. For each animal, instantaneous flow directions from all pixels within the cortical mask were binned into 15 equal-width angular bins to form a polar histogram. The radial axis was max normalized within each animal so that the largest bin equals 1. To quantify directional uniformity, the resultant vector length (R) was computed from each animal's angular histogram as the magnitude of the weighted vector sum of all bins, normalized by the total count. R ranges from 0 (uniform distribution across all directions) to 1 (all flow aligned in one direction). Group differences in R were assessed using a Wilcoxon rank-sum test.

Immunofluorescence staining

To assess the efficiency of AAV vector infection and the expression of GCaMP8s in the brains of Shank3B$^{+/+}$ and Shank3B$^{-/-}$ mice, immunofluorescence analysis was conducted with DAPI staining. Mice were euthanized at the end of the experiments using an overdose of pentobarbital sodium, followed by transcardial perfusion with saline, then formalin (1:10 dilution, FisherBrand) to fix the brain tissue. The brains were then carefully removed and post-fixed in 4% PFA overnight at 4°C. After fixation, the brain tissues were cryoprotected in 30% sucrose solution in distill water until they sank. Before the sectioning, brains were transferred from 4°C to -20°C by using 2-methylbutane and dry ice. Brains were sectioned coronally at a thickness of 30 µm using a cryostat (LEICA CM3050 S). Sections were collected and stored at -20°C until further processing. The sections were washed in 1xPBS for 15 min and mounted with antifade mounting medium with DAPI (VECTASHIELD, Biolynx) for 10 minutes at room temperature to label cell nuclei. After staining, the coverslip was placed on the slide and sealed with nail polish. Fluorescent images of the brain sections were captured using a fluorescence microscope (LEICA DMI6000 B). Imaging was first performed with a tile scan, then at 5x and 10x magnifications to visualize the tissue structure and DAPI-stained nuclei. ImageJ software was used for image processing.

Data Analysis

All calcium-imaging preprocessing and feature extraction were performed in MATLAB. Spontaneous recordings (12-bit, 10 Hz) were first band-pass filtered (0.1–4.99 Hz) using a zero-phase Chebyshev filter. A binary cortical mask drawn manually over a still frame via a GUI excluded non-cortical pixels, and global signal regression was applied to remove shared fluctuations. $\Delta F/F_0$ was computed by normalizing each pixel's fluorescence to its time-averaged baseline. The resulting $\Delta F/F_0$ stack was smoothed spatially with a 2D Gaussian filter (σ = 4 pixels). For ROI analysis, the processed still image was overlaid on the Allen Mouse Brain Atlas using a second GUI, which allowed manual selection of eleven 5×5-pixel ROIs. From each ROI's mean time course, spontaneous activity was summarized as the root-mean-square (RMS) over 15 minutes.

Sensory-evoked trials (8 or 20 s long, 10 Hz, 20–60 trials per condition) were processed similarly: $\Delta F/F_0$ was computed relative to the 3 s pre-stimulus baseline, and within each ROI we extracted peak response, trial-to-trial variability (standard deviation of peaks), baseline level, signal area above absolute

thresholds, signal-to-noise ratio (SNR; mean peak/SD of baseline), and inter-trial reliability (ITR; mean peak/SD of peak). To identify the most discriminative features, sensory-evoked metrics from all ROIs (peak, variability, baseline, reliability) were entered into a MATLAB logistic regression (fitglm, binomial), with 5-fold cross-validation for classification accuracy. In terms of resting-state activity, we first applied univariate logistic regression on RMS of each ROI to assess its individual ability to distinguish genotypes. This step identifies which single ROI carries the strongest predictive signal. We then employed LASSO-penalized logistic regression on RMS values from all ROIs to build a multivariate model that selects the minimal combination of regions while avoiding overfitting. The regularization parameter λ was chosen by five-fold cross-validation.

Statistical Analysis

Statistical analyses were conducted in GraphPad Prism 10 and MATLAB R2020a. For sensory-evoked data, we compared metrics across genotypes and stimulus intensities using two-way ANOVA (genotype x intensity) with Bonferroni-corrected post hoc tests; when a given metric was averaged across all intensities, genotypes were compared by unpaired t-test. All t-tests were two-tailed. Spontaneous RMS values were first subjected to three-way ANOVA (genotype x sex x ROI); because no significant sex effects or genotype x sex interactions were observed, male and female data were pooled and a two-way ANOVA (genotype x ROI) with Fisher's LSD post hoc tests was performed. All ANOVAs were preceded by Shapiro-Wilk tests for normality and Levene's tests for homogeneity of variance were used when assumptions were violated. For outcomes with a sex main effect and no genotype x sex interaction, we present sex-stratified and pooled estimates together.

For logistic regression models, p-values for individual coefficients were obtained via the Wald test in MATLAB's fitglm or lassoglm functions, with predictors considered significant at $p < 0.01$. All other statistical significance thresholds were set at $p < 0.05$.

Results

To verify that the efficiency of AAV-mediated GCaMP8s expression was comparable across genotypes, we quantified the mean raw fluorescence intensity from mesoscale imaging data and performed immunofluorescence analysis. Figure 1C shows that the overall fluorescence levels were similar between Shank3B$^{+/+}$ and Shank3B$^{-/-}$ mice across cortical ROIs. A two-way ANOVA (ROI x genotype) showed a significant main effect of ROI ($F(10, 264) = 14.17$, $p < 0.0001$), but neither the main effect of genotype ($F(1, 264) = 2.04$, $p = 0.15$) nor the interaction ($F(10, 264) = 1.49$, $p = 0.14$) was significant. Bonferroni-corrected post-hoc comparisons detected no genotype differences within individual ROIs. Representative coronal sections further demonstrate consistent GCaMP8s expression across Shank3B$^{+/+}$, Shank3B$^{+/-}$ and Shank3B$^{-/-}$ brains (Fig. 1D).

Visual-evoked cortical responses are enhanced in Shank3B $^{-/-}$ mice.

After the confirmation of availability of jGCaMP8s PHP.eB virus, we performed mesoscale calcium imaging with visual and whisker stimulation. We first quantified visual-evoked calcium responses in primary visual cortex (V1). Pseudocolor $\Delta F/F_0$ maps show visually-evoked activity across the dorsal cortex at 0, 100, 200, 300, 400, 500, and 600 ms after a 50 ms LED flash (Fig. 2A). Binarized maps ($\Delta F/F_0 > 0.6$) reveal that Shank3B$^{-/-}$ mice exhibit larger regions of suprathreshold activation compared with Shank3B$^{+/+}$ (Fig. 2B).

Time-resolved $\Delta F/F_0$ traces averaged over the V1 ROI confirm that Shank3B$^{-/-}$ mice have significantly higher peak responses than Shank3B$^{+/+}$ (Fig. 2C). Quantification across five light intensities (60, 100, 140, 180, 220 μW) shows a robust genotype effect (two-way ANOVA: genotype $F(1, 40) = 41.73$, $p < 0.0001$; Fig. 2D), and Shank3B$^{-/-}$ mice remain elevated when peaks are averaged across intensities (unpaired t-test: $t = 5.983$, $p < 0.0001$; Fig. 2E). When measuring V1 activation area above 0.6 $\Delta F/F_0$, Shank3B$^{-/-}$ mice again show larger areas than Shank3B$^{+/+}$, although this increase does not reach significance (two-way ANOVA: genotype $F(1,48) = 1.928$, $p = 0.1713$; Fig. 2F). Averaged across thresholds, there is a similar non-significant trend toward larger activation in mutants (unpaired t-test: $t = 1.163$, $p = 0.2498$; Fig. 2G). These results indicate that Shank3B$^{-/-}$ mice exhibit both greater amplitude and a tendency for expanded spatial extent of visual-evoked signals in V1.

Increased whisker-evoked responses in Shank3B$^{-/-}$ Mice

Pseudocolor $\Delta F/F_0$ maps reveal larger whisker-evoked responses in barrel cortex (BC) of Shank3B$^{-/-}$ mice than in Shank3B$^{+/+}$ (Fig. 3A). Binarized activation maps ($\Delta F/F_0 > 0.6$) confirm a broader suprathreshold area in Shank3B$^{-/-}$ BC (Fig. 3B). Peak $\Delta F/F_0$ across five whisker displacements (0.8, 1.6, 2.4, 3.2, 4.0 mm) is significantly higher in Shank3B$^{-/-}$ mice (two-way ANOVA: genotype $F(1, 45) = 55.51$, $p < 0.0001$; Fig. 3D), and remains elevated when averaged over all displacements (unpaired t-test: $t = 7.180$, $p < 0.0001$; Fig. 3E). Activated BC area above $\Delta F/F_0 = 0.6$ is also greater in Shank3B$^{-/-}$ mice (two-way ANOVA: genotype $F(1,54) = 16.77$, $p = 0.0001$; Fig. 3F, G). Thus, Shank3B$^{-/-}$ mice display exaggerated amplitude and spread of whisker-evoked responses in somatosensory cortex.

Increased variability and baseline fluctuations accompany exaggerated sensory responses in Shank3B$^{-/-}$ mice

Having established that Shank3B$^{-/-}$ mice exhibit exaggerated sensory-evoked responses at the population level, we next examined whether these responses also differ in their trial-to-trial stability. To this end, we quantified variability and reliability of whisker- and visual-evoked $\Delta F/F_0$ signals using five complementary response metrics that capture response magnitude, baseline fluctuations, and response consistency (Fig. 4a,b). All metrics shown in Fig. 4 were computed at the animal level using responses evoked by the highest stimulus intensity.

Inspection of trial-by-trial response patterns immediately revealed qualitative differences between genotypes (Fig. 4c). In Shank3B$^{+/+}$ mice, evoked responses were relatively consistent across repeated trials, with stable baselines and reproducible response peaks. In contrast, Shank3B$^{-/-}$ mice showed pronounced fluctuations both before and during stimulus presentation, resulting in greater dispersion of evoked responses across trials for both whisker and visual stimulation.

Quantitative analysis confirmed these observations. For whisker stimulation, Shank3B$^{-/-}$ mice exhibited not only larger peak response amplitudes but also substantially increased trial-to-trial variability of peak responses and elevated baseline fluctuations relative to Shank3B$^{+/+}$ controls (Fig. 4d). Despite this increase in variability, inter-trial reliability was higher in Shank3B$^{-/-}$ mice, reflecting the dominance of larger mean response amplitudes over the dispersion of peak responses. Signal-to-noise ratio, however, did not differ reliably between genotypes, indicating that increased baseline fluctuations partially offset the amplification of evoked responses.

For visual stimulation, genotype effects were more selective (Fig. 4e). At this animal-averaged summary-metric level, peak response amplitude did not show a robust genotype difference. However, Shank3B$^{-/-}$ mice exhibited increased baseline fluctuations and greater dispersion of variability-related response measures. In contrast, signal-to-noise ratio and inter-trial reliability were not significantly altered, indicating that increased variability in the visual modality has limited impact on response reliability.

To compare genotype effects across response features and sensory modalities, group differences were summarized using standardized effect sizes (Hedges' g; Fig. 4f). Across both whisker and visual stimulation, genotype-associated shifts were more pronounced for variability-related measures, particularly baseline fluctuations and trial-to-trial dispersion of peak responses, whereas effects on signal-to-noise ratio and inter-trial reliability were smaller and modality dependent.

We next asked whether the increased response variability observed in Shank3B$^{-/-}$ mice could be accounted for by differences in response amplitude. In Shank3B$^{+/+}$ mice, variability of peak responses scaled with mean response amplitude, providing a reference amplitude-variability relationship for each sensory modality (Fig. 4g). When responses were evaluated relative to this reference, Shank3B$^{-/-}$ mice exhibited a clear increase in the spread of residuals during whisker stimulation, indicating greater trial-to-trial variability than expected from response amplitude alone. A similar pattern was observed for visual stimulation; however, the broadening of the residual distribution was comparatively modest.

Together, these results demonstrate that exaggerated sensory responses in Shank3B$^{-/-}$ mice are accompanied by fundamental alterations in response stability. Rather than reflecting a simple amplification of otherwise stable sensory signals, Shank3B deletion is associated with increased baseline fluctuations and excessive trial-to-trial variability, with modality-specific consequences for response reliability.

Faster propagation speed and preserved directional symmetry in Shank3B$^{-/-}$ mice.

Using CLG optical flow, we derived a per-animal average propagation speed (mm/s) from stimulus onset to the peak of the $\Delta F/F_0$ response. Shank3B$^{-/-}$ mice showed significantly higher average speed than Shank3B$^{+/+}$ for both visual stimulation (Welch's t-test: $t(11.49) = 2.365$, $p = 0.037$; Fig. 5a) and whisker stimulation (Mann-Whitney $U = 16$, $p = 0.032$; Fig. 5f). Sex-stratified analyses are presented in Supplementary Fig. 3; because no significant genotype x sex interaction was detected (two-way ANOVA; visual: $F(1, 14) = 1.50$, $p = 0.24$; whisker: $F(1, 14) = 1.15$, $p = 0.71$), male and female data were pooled.

To characterize the spatial geometry of wave propagation, we computed polar histograms of instantaneous flow direction for each genotype (Fig. 5b-d, g-i). Both Shank3B$^{+/+}$ and Shank3B$^{-/-}$ exhibited broadly distributed directional profiles consistent with radial expansion from the activation site. The resultant vector length (R), which ranges from 0 (uniform) to 1 (unidirectional), did not differ between genotypes for either visual (Shank3B$^{+/+}$: $R = 0.286 \pm 0.066$; Shank3B$^{-/-}$: $R = 0.415 \pm 0.080$; mean ± SEM; Mann-Whitney $U = 24$, $p = 0.155$; Fig. 5e) or whisker stimulation (Shank3B$^{+/+}$: $R = 0.319 \pm 0.088$; Shank3B$^{-/-}$: $R = 0.231 \pm 0.054$; Mann-Whitney $U = 34$, $p = 0.587$; Fig. 5j). Thus, while Shank3B$^{-/-}$ mice exhibit faster cortical propagation, the directional profile of wave spread is preserved.

Predictive modeling of genotype from sensory-evoked features

To assess whether sensory-evoked features are associated with Shank3B genotype, we first performed univariate logistic regression for each predictor-Response_Z (peak $\Delta F/F_0$), STD_response_Z (variability of peak), and Baseline_Z (baseline $\Delta F/F_0$) separately for visual and whisker modalities (Table 1). Five-fold cross-validation yielded CV-AUC and accuracy values shown in Table 1. In the visual paradigm, Response_Z achieved a CV-AUC of 0.818 (75% accuracy, slope = 1.43, $p < 0.001$), STD_response_Z gave 0.752 (65% accuracy, slope = 1.08, $p < 0.001$), and Baseline_Z gave 0.794 (70% accuracy, slope = 1.58, $p < 0.001$). In the whisker paradigm, Baseline_Z was most strongly associated with genotype (CV-AUC = 0.934; 80% accuracy; slope = 2.88; $p < 0.001$), while Response_Z (CV-AUC = 0.866; 79% accuracy; slope = 2.22; $p < 0.001$) and STD_response_Z (CV-AUC = 0.836; 74% accuracy; slope = 1.67; $p < 0.001$) also showed significant associations.

Next, we combined all three predictors into a multivariate logistic regression within each modality, yielding CV-AUCs of 0.808 (visual) and 0.924 (whisker). Finally, to determine which modality and feature carried the strongest genotype-association across sensory domains, we fitted a combined model that included modality (visual vs. whisker) as a fixed factor alongside the three Z-scored predictors (supplemental materials). In this combined analysis, whisker-evoked Baseline_Z emerged as the single most significant predictor of Shank3B$^{-/-}$ status. All p-values for individual coefficients derive from Wald tests, and multivariate p-values are from likelihood-ratio tests against an intercept-only model. Further validation procedures are described in Supplemental methods.

Table 1
Univariate and multivariate logistic regression to predict the genotypes

Modalities	Predictor	CV-AUC	Slope	ACC	p-value
Vision	Response_Z	0.818	1.43	75%	< 0.001
	STD_response_Z	0.752	1.08	65%	< 0.001
	Baseline_Z	0.794	1.58	70%	< 0.001
	Multivariate	0.808	/	/	< 0.001
Whisker	Response_Z	0.866	2.22	79%	< 0.001
	STD_response_Z	0.836	1.67	74%	< 0.001
	Baseline_Z	0.934	2.88	80%	< 0.001
	Multivariate	0.924	/	/	< 0.001

Separate univariate logistic regression models were trained to classify Shank3B$^{+/+}$ vs. Shank3B$^{-/-}$ mice based on three z-scored metrics derived from visual or whisker stimulation: peak response amplitude (Response_Z), trial-to-trial variability (STD_response_Z), and baseline fluctuations (Baseline_Z). All predictor variables were standardized within modality prior to regression.

CV-AUC indicates the cross-validated area under the ROC curve (5-fold cross-validation). Slope refers to the log-odds coefficient of the predictor. ACC represents the cross-validated classification accuracy. *p*-values were obtained from likelihood-ratio tests comparing each model to a null model.

Multivariate models included all three predictors simultaneously. Slope and ACC values are omitted for the multivariate model due to potential collinearity among predictors, which limits interpretability of individual coefficients.

Spontaneous cortical hyperactivity in Shank3B $^{-/-}$ mice predicts genotype, with strongest effects in barrel and secondary somatosensory cortex.

To determine whether spontaneous cortical activity differed by genotype, sex, and region, we performed a three-way repeated-measures ANOVA (Genotype x sex * ROI) on RMS values across eleven cortical regions. Figure 6a shows the schematic of cortical regions in the imaging field of view, example $\Delta F/F_0$ trace from one ROI, and definition of RMS used to quantify spontaneous activity. A significant main effect of genotype was found ($F(1, 22) = 6.66$, $p = 0.0171$, Fig. 6b), indicating higher global RMS activity in Shank3B$^{-/-}$ mice. No significant main effect of sex ($F(1, 22) = 0.0897$, $p = 0.767$) or genotype x sex interaction ($F(1, 22) = 0.0856$, $p = 0.773$) was detected. A significant main effect of ROI was present ($F(10,220) = 54.52$, $p < 0.0001$; Greenhouse-Geisser corrected), as well as a significant genotype * ROI interaction ($F(10, 220) = 4.43$, $p = 0.0306$; GG corrected). The three-way interaction (Genotype x sex * ROI) was not significant ($F(10, 220) = 0.123$, $p = 0.999$). To visualize sex-specific effect sizes, we plotted post hoc genotype differences (Shank3B$^{+/+}$ - Shank3B$^{-/-}$) with 95% confidence intervals separately for females (Fig. 6c) and males (Fig. 6d). Given the absence of sex-related effects or interactions, male and female animals were pooled in subsequent comparisons. Shank3B$^{-/-}$ mice exhibited significantly higher

spontaneous activity than Shank3B$^{+/+}$ controls in most ROIs, when pooled RMS values were compared across genotype and region (Fig. 6e). A two-way repeated-measures ANOVA (genotype x ROI) revealed a main effect of genotype ($F(1, 24) = 7.83$, $p = 0.00996$) and a main effect of ROI ($F(1.501, 36.02) = 57.49$, $p < 0.0001$), as well as a significant genotype x ROI interaction ($F(10, 240) = 5.07$, $p < 0.0001$). Bonferroni-corrected post hoc tests showed elevated RMS in Shank3B$^{-/-}$ versus Shank3B$^{+/+}$ at PFC ($p = 0.0080$), CG ($p = 0.0012$), M2 ($p = 0.049$), M1 ($p = 0.013$), FL ($p = 0.026$), HL ($p = 0.0072$), BC ($p = 0.0046$), S2 ($p = 0.0090$), RS ($p = 0.01$), and V1 ($p = 0.0011$), whereas AU did not differ significantly.

These findings indicate that, in a mixed-sex cohort, Shank3B$^{-/-}$ mice display a global increase in spontaneous cortical activity, consistent with the hyperexcitable baseline that likely underlies their exaggerated sensory-evoked responses.

To test whether resting-state activity could predict genotype, we performed univariate logistic regression using z-scored RMS from each ROI. Several ROIs showed significant associations with Shank3B$^{-/-}$ status (Fig. 6f). The strongest predictors were BC (log-odds ratio = 2.939, $p = 0.011$) and S2 (log-odds ratio = 7.584, $p = 0.013$), each yielding high cross-validated AUCs (0.78 and 0.80, respectively; Fig. 6g). Other significant ROIs included AU, PFC, M2, M1, FL, RS, and HL, indicating that, on their own, somatosensory areas provide the most reliable discrimination of genotype. Multivariate LASSO logistic regression was used to identify a minimal predictor set. Only BC and S2 retained non-zero coefficients at the optimal penalty (Fig. 6h). The final model achieved a 5-fold cross-validated AUC of 0.704 (Fig. 6i).

These results indicate that spontaneous hyperactivity in Shank3B$^{-/-}$ mice is widespread but strongest in somatosensory regions, particularly BC and S2. Moreover, this resting-state signature is sufficient to predict genotype with reasonable accuracy, supporting its value as a diagnostic biomarker in this model.

Our optical-flow measurements indicate faster spread in Shank3B$^{-/-}$ cortex (Fig. 5). These propagation-speed results therefore extend the picture from stronger responses to faster network deployment and motivate the mechanistic considerations below.

Discussion

We used wide-field calcium imaging to compare sensory-evoked activity in Shank3B$^{-/-}$ and Shank3B$^{+/+}$ mice. In both V1 and barrel cortex, mutants exhibited larger peak $\Delta F/F_0$ signals, expanded activation areas, and increased trial-to-trial variability demonstrating that Shank3B loss produces hyperactive, noisy, and inconsistent sensory responses.

Optical-flow analysis adds a dynamic dimension: propagation speed is significantly faster in Shank3B$^{-/-}$ cortex for both visual and whisker stimulation (Fig. 5a and f). Direction analysis revealed broadly distributed propagation profiles in both genotypes, with no significant difference in directional consistency (Fig. 5e and j), suggesting that the underlying wave geometry is preserved. Together with

the larger peaks and activation areas (Figs. 2–3), the speed increase without directional disruption points to a higher-gain operating state.

This phenotype reflects a dual hit on cortical excitation - inhibition balance. Shank3 deletion impairs postsynaptic scaffolding at glutamatergic synapses augmenting AMPA/NMDA currents, reducing spine density, and boosting pyramidal-cell drive (22, 23, 24, 25). In addition to synaptic defects, non-synaptic channelopathies also play a role, with broad HCN channel dysfunction elevating cortical excitability (26) and HCN2 channelopathy in Shank3 exon13-19 mutants causally driving barrel-cortex sensory hypersensitivity which is absent in exon4-9 models and highlighting isoform-specific circuit perturbations (27). Nevertheless, further work is needed to map how different Shank3 isoforms engage distinct excitatory and channel mechanisms.

Other studies emphasize inhibitory-neuron deficits in ASD models. Interneuron-restricted Shank3 loss in vS1 diminishes GABAergic firing and disinhibits pyramidal output (22), and pharmacological enhancement of GABA_A receptors restores inhibition and improves autistic-like behaviors (28). How excitatory, channel, and inhibitory abnormalities converge to shape network dynamics remains an important question. Long-range connectivity changes likely reinforce local hyperexcitability. Shank3 mutations impair thalamocortical relay (27), weaken S1-hippocampal coupling (29), and reduce prefrontal connectivity, all of which may feed back to destabilize resting-state RMS and sensory gain. Taken together, these results suggest that Shank3 loss may disrupt cortical excitation-inhibition balance through synaptic scaffolding dysfunction, isoform-specific HCN2 channelopathies, impaired GABAergic inhibition and altered long-range connectivity, although further studies will be needed to clarify the relative contributions of each mechanism.

Notably, baseline RMS fluctuations in BC and S2 emerged as the strongest predictors of Shank3B genotype. Clinically, Dinstein et al. (2012) reported that individuals with ASD exhibit the same average BOLD response amplitudes as controls yet display substantially higher trial-to-trial variability (30). This increased variability drives down the fMRI-derived signal-to-noise ratio during sensory stimulation, even though resting-state reliability remains unchanged. In contrast, our Shank3B$^{-/-}$ mice show higher whisker-evoked SNR and ITR compared to Shank3B$^{+/+}$, while visual cortical measures remain equivalent. This divergence likely reflects the concurrent rise in both $\Delta F/F_0$ peaks and baseline fluctuations in our calcium recordings-when peak values increase slightly more than baseline noise, the computed signal-to-noise ratio increases. Additional contributors include light isoflurane anesthesia, which shifts network gain, and our use of fast intracellular calcium transients rather than awake hemodynamic signals, both of which shape noise and gain differently across modalities. Moreover, using 500-millisecond, 20-Hz whisker trains instead of single 50-millisecond visual flashes favors greater temporal summation in barrel cortex, boosting signal-to-noise there without altering visual cortex reliability. Finally, our predictive models show that whisker-evoked baseline activity is the single best Shank3B genotype predictor, and that at rest only BC and S2 RMS remain robust. A study reported S1 hyperconnectivity and tactile deficits in Cntnap2$^{-/-}$ mice (31), whereas the other study found that V1 responses largely spared (32). These parallel findings in other ASD models hint at a somatosensory bias. Testing this idea definitively will

require within-model comparisons under matched conditions, but our resting-state biomarkers in BC and S2 provide a promising entry point for such studies.

As demonstrated in early postnatal somatosensory cortex, emergent synchronous GABAergic activity in layer IV barrel field provides an early network window for detecting later sensory-pathway disruptions (33). When these oscillations go awry, they lead to bidirectional increases in both baseline and stimulus-evoked activity within S1 (33).

In 3-7-year-old children with ASD, increased gray-matter volume in the postcentral gyrus and heightened resting-state functional connectivity with parietal-occipital association regions correlate significantly with sensory hypersensitivity and social behavior impairments (34), while DTI reveals radial diffusivity increases in thalamocortical pathways linked to repetitive behaviors (35).

In Shank3B$^{+/-}$ mice, network hyperconnectivity originates first in the barrel-field cortex during the juvenile stage and then progressively spreads across the dorsal cortex; this aberrant pattern is most pronounced in the awake state and largely normalizes under anesthesia (36).

Together, these convergent findings highlight BC/S2 network alterations as actionable biomarkers for early ASD diagnosis and monitoring of therapeutic interventions.

Resting-state baseline excitability interacts with sensory-evoked responses in a measurement modality- and frequency-dependent manner. In addition to propounding changes in BC and S2 RMS, the strongest genotype predictors, we also observed increased RMS across nearly all ROIs, pointing to a brain-wide increase in baseline excitability. Resting-state fluctuations are known to set the gain for subsequent sensory responses that higher baseline activity can increase peak responses (37). By contrast, in vivo whole-cell recordings in rodent barrel cortex showed that whisker-evoked synaptic potentials and spikes are actually suppressed during spontaneous UP-states, accounting for much of the trial-to-trial variability (38). Human fMRI then revealed a negative interaction between baseline and evoked BOLD amplitude, such that higher ongoing activity leads to reduced evoked responses (39). More recently, large-scale MEG/EEG work has uncovered frequency-dependent effects that high-frequency baseline power predicts greater evoked desynchronization, whereas low-frequency power correlates positively with event-related synchronization (40). In parallel, our low-frequency (0.1–4.99 Hz) calcium imaging data reveal a positive coupling between spontaneous fluctuations and sensory-evoked $\Delta F/F_0$ responses, consistent with the frequency-dependent relationships reported in human studies. Together, these findings indicate that the relationship between spontaneous and evoked signals is not fixed but varies with measurement modality, cortical state, frequency band, and neural circuit, underscoring the need to interpret spontaneous-evoked interactions in the context of each specific experimental paradigm. In our data, the globally elevated RMS likely primes cortical networks for the exaggerated, noisy evoked signals we report, suggesting a tight coupling between spontaneous and stimulus-driven dynamics.

Sex-specific analyses reveal that female cortical networks maintain high baseline excitability that may buffer sensory dysfunction. Human imaging studies have reported sex-specific alterations in resting-

state connectivity in ASD (41, 42). In Shank3B mutant mice, previous slice work has documented sex-dependent synaptic deficits (43), yet no in vivo data existed on how these translate to mesoscale activity. By pooling sexes only after ruling out significant interactions in a three-way ANOVA, we show that the same BC and S2 robustly predict Shank3B status regardless of sex, while females maintain a uniquely high baseline that may buffer against overt synaptic dysfunction. Analysis by sex (see Supplementary Materials) revealed that female Shank3B$^{+/+}$ and Shank3B$^{-/-}$ mice consistently exhibited higher resting-state RMS than their male counterparts, yet paradoxically displayed smaller sensory-evoked $\Delta F/F_0$ peaks. This dissociation implies that female cortical networks may reside more often in a depolarized up-state, raising tonic activity while constraining the phasic response amplitude (44, 45). Moreover, while males showed clear genotype-dependent increases in baseline RMS, females did not, suggesting an intrinsic resilience of female circuits to Shank3B loss. Such resilience echoes the female protective effect in ASD, whereby females require a greater genetic burden to express clinical symptoms, and points to elevated baseline excitability as a circuit-level mechanism modulating phenotypic penetrance (46).

One important limitation of our study is that all imaging was performed under light isoflurane anesthesia, which may alter baseline excitability and sensory-evoked dynamics relative to the awake state. We also focused solely on the Shank3B model and two primary sensory regions, so the generality of BC and S2 biomarkers across other ASD genotypes and cortical areas remains to be established.

Future work should address these gaps by performing longitudinal, awake imaging to capture naturalistic sensory processing, combining mesoscale $\Delta F/F_0$ measurements with two-photon or electrode recordings to dissect excitatory versus inhibitory and cell-type mechanisms. Integrating our BC and S2 RMS biomarkers with behavioral assays and human neuroimaging will be essential to validate their translational potential. Finally, targeted optogenetic or chemogenetic manipulations of BC-S2 circuits in both sexes could test causally whether normalizing baseline excitability ameliorates sensory and social phenotypes. Together, these findings underscore the translational relevance of our RMS-based approach for informing future ASD diagnostics and interventions.

In conclusion, our study demonstrates that Shank3B loss leads to widespread cortical hyperactivity, with BC and S2 emerging as key regions where resting-state RMS fluctuations are both robustly elevated and predictive of genotype. These metrics reflect converging excitatory, inhibitory, and intrinsic mechanisms of circuit dysfunction and serve as reliable mesoscale biomarkers in this ASD model. Future work integrating these circuit-level signals with behavioral phenotypes and human imaging markers may pave the way for translationally meaningful diagnostic and therapeutic strategies.

Declarations

Author Contribution

AWC and ZY conceived the study and designed the analytical framework. ZY performed the majority of the experiments and data acquisition, led the data analysis, and wrote the initial manuscript. YM contributed to experimental data acquisition and provided surgical support. RZ developed analysis code and contributed to data analysis. IRW provided equipment and experimental infrastructure, contributed to interpretation of the findings, and provided critical intellectual input on the manuscript. AWC secured project funding, supervised the study, contributed to data interpretation and analytical development, and critically revised the manuscript. All authors reviewed and approved the submitted version.

Acknowledgement

We thank Tricia Kent for her assistance with animal husbandry, colony management, and laboratory management. This work was supported by a Brain Canada Foundation Future Leaders Award (AWC), a Puzzles of the Mind Award from the Scottish Rite Charitable Foundation (AWC), and an NSERC Discovery Grant (RGPIN-2020-05988; AWC). The support provided by the China Scholarship Council (CSC) is gratefully acknowledged (ZY).

Data Availability

Data are available from the corresponding author upon reasonable request.

Code Availability

Codes used for analysis are available from the corresponding author upon reasonable request.

Data availability

Data used to generate graphs and plots in the main figures is provided in the Supplemental Data file. Data are available from the corresponding author upon reasonable request.

Authors’ contribution

AWC and ZY conceived the study and designed the analytical framework. ZY performed the majority of the experiments and data acquisition, led the data analysis, and wrote the initial manuscript. YM contributed to experimental data acquisition and provided surgical support. RZ developed analysis code and contributed to data analysis. IRW provided equipment and experimental infrastructure, contributed to interpretation of the findings, and provided critical intellectual input on the manuscript. AWC secured project funding, supervised the study, contributed to data interpretation and analytical development, and critically revised the manuscript. All authors reviewed and approved the submitted version.

References

1. Diagnostic and statistical manual of mental disorders: DSM-5™, 5th ed. Arlington, VA, US: American Psychiatric Publishing, Inc.; 2013. xliv, 947-xliv, p.
2. Grapel JN, Cicchetti DV, Volkmar FR. Sensory features as diagnostic criteria for autism: sensory features in autism. Yale J Biol Med. 2015;88(1):69–71.
3. Werling DM, Geschwind DH. Sex differences in autism spectrum disorders. Current Opinion in Neurology. 2013;26(2).
4. Lai M-C, Lombardo MV, Baron-Cohen S. Autism. The Lancet. 2014;383(9920):896–910.
5. Little LM, Dean E, Tomchek S, Dunn W. Sensory Processing Patterns in Autism, Attention Deficit Hyperactivity Disorder, and Typical Development. Physical & Occupational Therapy In Pediatrics. 2018;38(3):243–54.
6. Crasta JE, Salzinger E, Lin M-H, Gavin WJ, Davies PL. Sensory Processing and Attention Profiles Among Children With Sensory Processing Disorders and Autism Spectrum Disorders. Frontiers in Integrative Neuroscience. 2020;14.
7. Ben-Sasson A, Hen L, Fluss R, Cermak SA, Engel-Yeger B, Gal E. A Meta-Analysis of Sensory Modulation Symptoms in Individuals with Autism Spectrum Disorders. Journal of Autism and Developmental Disorders. 2009;39(1):1–11.
8. Schulz SE, Stevenson RA. Sensory hypersensitivity predicts repetitive behaviours in autistic and typically-developing children. Autism. 2019;23(4):1028–41.
9. Takarae Y, Sablich SR, White SP, Sweeney JA. Neurophysiological hyperresponsivity to sensory input in autism spectrum disorders. Journal of Neurodevelopmental Disorders. 2016;8(1):29.
10. Ujiie Y, Takahashi K. Associations between self-reported social touch avoidance, hypersensitivity, and autistic traits: Results from questionnaire research among typically developing adults. Personality and Individual Differences. 2022;184:111186.
11. Osório JMA, Rodríguez-Herreros B, Richetin S, Junod V, Romascano D, Pittet V, et al. Sex differences in sensory processing in children with autism spectrum disorder. Autism Research. 2021;14(11):2412–23.
12. Napolitano A, Schiavi S, La Rosa P, Rossi-Espagnet MC, Petrillo S, Bottino F, et al. Sex Differences in Autism Spectrum Disorder: Diagnostic, Neurobiological, and Behavioral Features. Frontiers in Psychiatry. 2022;Volume 13–2022.
13. Naisbitt S, Kim E, Tu JC, Xiao B, Sala C, Valtschanoff J, et al. Shank, a Novel Family of Postsynaptic Density Proteins that Binds to the NMDA Receptor/PSD-95/GKAP Complex and Cortactin. Neuron. 1999;23(3):569–82.
14. Zhou Y, Kaiser T, Monteiro P, Zhang X, Van der Goes MS, Wang D, et al. Mice with Shank3 Mutations Associated with ASD and Schizophrenia Display Both Shared and Distinct Defects. Neuron. 2016;89(1):147–62.
15. Peça J, Feliciano C, Ting JT, Wang W, Wells MF, Venkatraman TN, et al. Shank3 mutant mice display autistic-like behaviours and striatal dysfunction. Nature. 2011;472(7344):437–42.

16. Bozdagi O, Sakurai T, Papapetrou D, Wang X, Dickstein DL, Takahashi N, et al. Haploinsufficiency of the autism-associated Shank3 gene leads to deficits in synaptic function, social interaction, and social communication. Molecular Autism. 2010;1(1):15.
17. Medina E, Rempe MJ, Muheim C, Schoch H, Singletary K, Ford K, et al. Sex differences in sleep deficits in mice with an autism-linked Shank3 mutation. Biology of Sex Differences. 2024;15(1):85.
18. Tripathi MK, Ojha SK, Kartawy M, Khaliulin I, Hamoudi W, Amal H. Mutations associated with autism lead to similar synaptic and behavioral alterations in both sexes of male and female mouse brain. Scientific Reports. 2024;14(1):10.
19. Vanni MP, Chan AW, Balbi M, Silasi G, Murphy TH. Mesoscale Mapping of Mouse Cortex Reveals Frequency-Dependent Cycling between Distinct Macroscale Functional Modules. The Journal of Neuroscience. 2017;37(31):7513–33.
20. Zahacy R, Ma Y, Winship IR, Jackson J, Chan AW. Claustrum modulation drives altered prefrontal cortex dynamics and connectivity. Communications Biology. 2024;7(1):1556.
21. Afrashteh N, Inayat S, Mohsenvand M, Mohajerani MH. Optical-flow analysis toolbox for characterization of spatiotemporal dynamics in mesoscale optical imaging of brain activity. NeuroImage. 2017;153:58–74.
22. Chen Q, Deister CA, Gao X, Guo B, Lynn-Jones T, Chen N, et al. Dysfunction of cortical GABAergic neurons leads to sensory hyper-reactivity in a Shank3 mouse model of ASD. Nature Neuroscience. 2020;23(4):520–32.
23. Verpelli C, Dvoretskova E, Vicidomini C, Rossi F, Chiappalone M, Schoen M, et al. Importance of Shank3 Protein in Regulating Metabotropic Glutamate Receptor 5 (mGluR5) Expression and Signaling at Synapses *. Journal of Biological Chemistry. 2011;286(40):34839–50.
24. Kim S, Kim Y-E, Song I, Ujihara Y, Kim N, Jiang Y-H, et al. Neural circuit pathology driven by Shank3 mutation disrupts social behaviors. Cell Reports. 2022;39(10):110906.
25. Zhu F, Shi Q, Jiang Y-h, Zhang YQ, Zhao H. Impaired synaptic function and hyperexcitability of the pyramidal neurons in the prefrontal cortex of autism-associated Shank3 mutant dogs. Molecular Autism. 2024;15(1):9.
26. Yi F, Danko T, Botelho SC, Patzke C, Pak C, Wernig M, et al. Autism-associated SHANK3 haploinsufficiency causes Ih channelopathy in human neurons. Science. 2016;352(6286):aaf2669.
27. Guo B, Liu T, Choi S, Mao H, Wang W, Xi K, et al. Restoring thalamocortical circuit dysfunction by correcting HCN channelopathy in < em>Shank3 mutant mice. Cell Reports Medicine. 2024;5(5).
28. Pagano J, Landi S, Stefanoni A, Nardi G, Albanesi M, Bauer HF, et al. Shank3 deletion in PV neurons is associated with abnormal behaviors and neuronal functions that are rescued by increasing GABAergic signaling. Molecular Autism. 2023;14(1):28.
29. Pagani M, Bertero A, Liska A, Galbusera A, Sabbioni M, Barsotti N, et al. Deletion of Autism Risk Gene Shank3 Disrupts Prefrontal Connectivity. The Journal of Neuroscience. 2019;39(27):5299–310.

30. Dinstein I, Heeger David J, Lorenzi L, Minshew Nancy J, Malach R, Behrmann M. Unreliable Evoked Responses in Autism. Neuron. 2012;75(6):981–91.
31. Balasco L, Pagani M, Pangrazzi L, Chelini G, Viscido F, Chama AGC, et al. Somatosensory cortex hyperconnectivity and impaired whisker-dependent responses in Cntnap2–/– mice. Neurobiology of Disease. 2022;169:105742.
32. Townsend LB, Smith SL. Genotype- and sex-dependent effects of altered Cntnap2 expression on the function of visual cortical areas. Journal of Neurodevelopmental Disorders. 2017;9(1):2.
33. Iannone AF, De Marco García NV. The Emergence of Network Activity Patterns in the Somatosensory Cortex – An Early Window to Autism Spectrum Disorders. Neuroscience.2021;466:298–309.
34. Wang J, Fu K, Chen L, Duan X, Guo X, Chen H, et al. Increased Gray Matter Volume and Resting-State Functional Connectivity in Somatosensory Cortex and their Relationship with Autistic Symptoms in Young Boys with Autism Spectrum Disorder. Frontiers in Physiology. 2017;Volume 8–2017.
35. Duerden EG, Card D, Roberts SW, Mak-Fan KM, Chakravarty MM, Lerch JP, et al. Self-injurious behaviours are associated with alterations in the somatosensory system in children with autism spectrum disorder. Brain Structure and Function. 2014;219(4):1251–61.
36. Montagni E, Ambrosone M, Martello A, Curti L, Polverini F, Baroncelli L, et al. Age-dependent cortical overconnectivity in Shank3 mice is reversed by anesthesia. Translational Psychiatry. 2025;15(1):154.
37. Arieli A, Shoham D, Hildesheim R, Grinvald A. Coherent spatiotemporal patterns of ongoing activity revealed by real-time optical imaging coupled with single-unit recording in the cat visual cortex. Journal of Neurophysiology. 1995;73(5):2072–93.
38. Petersen CCH, Hahn TTG, Mehta M, Grinvald A, Sakmann B. Interaction of sensory responses with spontaneous depolarization in layer 2/3 barrel cortex. Proceedings of the National Academy of Sciences. 2003;100(23):13638-43.
39. He BJ. Spontaneous and Task-Evoked Brain Activity Negatively Interact. The Journal of Neuroscience. 2013;33(11):4672.
40. Wainio-Theberge S, Wolff A, Northoff G. Dynamic relationships between spontaneous and evoked electrophysiological activity. Communications Biology. 2021;4(1):741.
41. Alaerts K, Swinnen SP, Wenderoth N. Sex differences in autism: a resting-state fMRI investigation of functional brain connectivity in males and females. Social Cognitive and Affective Neuroscience. 2016;11(6):1002–16.
42. Smith REW, Avery JA, Wallace GL, Kenworthy L, Gotts SJ, Martin A. Sex Differences in Resting-State Functional Connectivity of the Cerebellum in Autism Spectrum Disorder. Frontiers in Human Neuroscience. 2019;Volume 13–2019.
43. Cai G, Wang M, Wang S, Liu Y, Zhao Y, Zhu Y, et al. Brain mGluR5 in Shank3B–/– Mice Studied With in vivo [18F]FPEB PET Imaging and ex vivo Immunoblotting. Frontiers in Psychiatry. 2019;Volume 10–2019.
44. Hasenstaub A, Sachdev RNS, McCormick DA. State Changes Rapidly Modulate Cortical Neuronal Responsiveness. The Journal of Neuroscience. 2007;27(36):9607.

45. Sigalas C, Konsolaki E, Skaliora I. Sex differences in endogenous cortical network activity: spontaneously recurring Up/Down states. Biology of Sex Differences. 2017;8(1):21.
46. Wigdor EM, Weiner DJ, Grove J, Fu JM, Thompson WK, Carey CE, et al. The female protective effect against autism spectrum disorder. Cell Genomics. 2022;2(6).

Figures

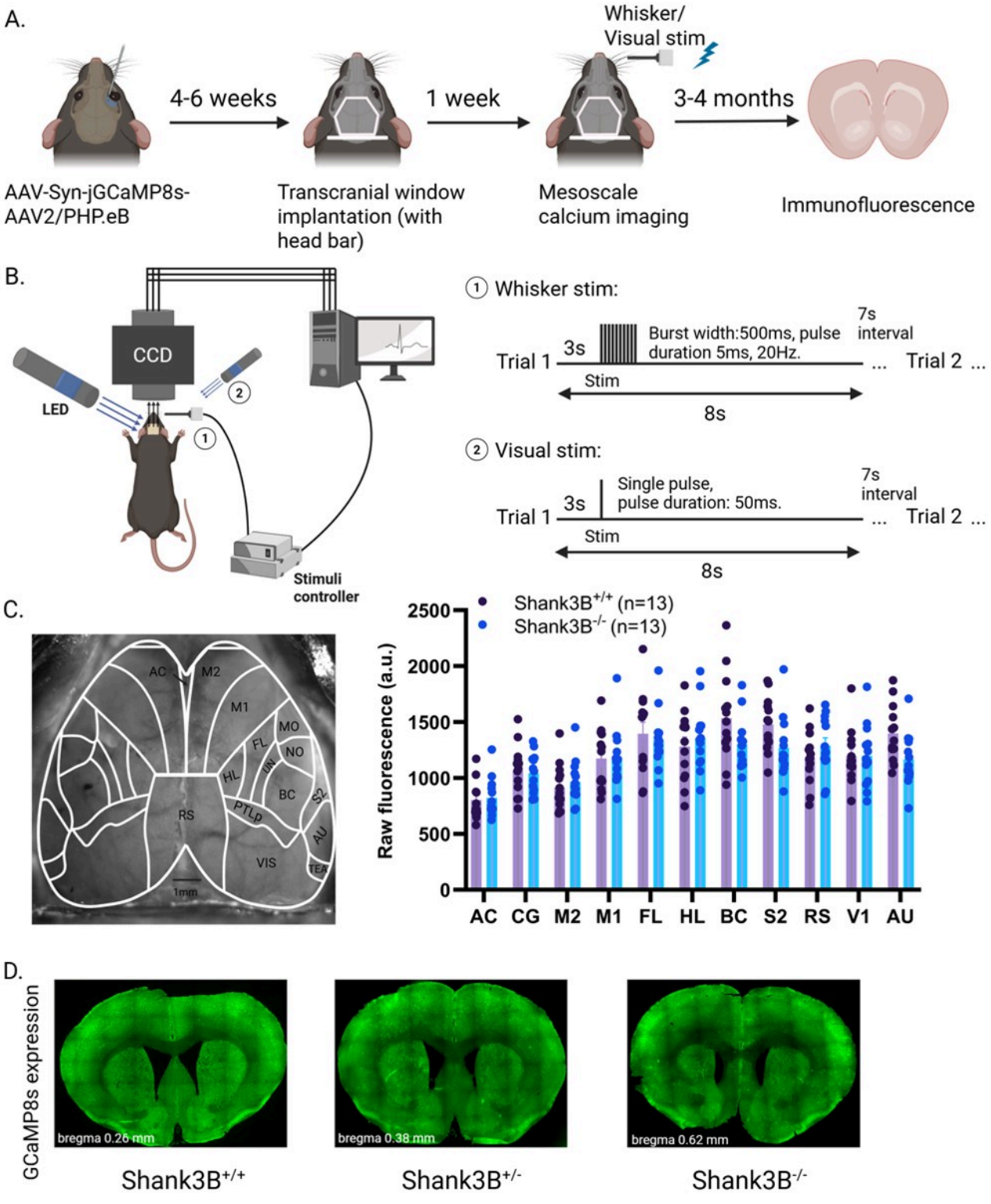

Figure 1

Experimental workflow, mesoscale imaging setup, and verification of GCaMP8s expression.

(A) Experimental timeline: Mice received retro-orbital injections of AAV-Syn-jGCaMP8s (AAV2/PHP.eB) to induce cortical expression of GCaMP8s. After an expression period of 4-6 weeks, transcranial windows with head bars were surgically implanted. Mesoscale calcium imaging was performed one week after implantation using whisker or visual stimulation paradigms over a period of 3-4 months, followed by terminal immunofluorescence analysis. (B) Mesoscale imaging setup and stimulation paradigms. Whisker stimulation: 500 ms burst at 20 Hz (5 ms pulse). Visual stimulation: single 50 ms light pulse. Inter-trial interval: 7 s. (C) Left: cortical ROI map used for analysis. Right: mean raw GCaMP8s fluorescence (a.u.) across ROIs for Shank3B+/+ and Shank3B mice (mixed sex). Bars show mean ± SEM; sample sizes are indicated in the panel. Anterior cingulate cortex (AC), cingulate cortex (CG), secondary motor cortex (M2), primary motor cortex (M1), forelimb area (FL), hindlimb area (HL), barrel cortex (BC), secondary somatosensory cortex (S2), retrosplenial cortex (RS), primary visual cortex (V1), and auditory cortex (AU). (D) Representative coronal sections illustrating GCaMP8s fluorescence in Shank3B+/+, Shank3B+/- and Shank3B-/- brains.

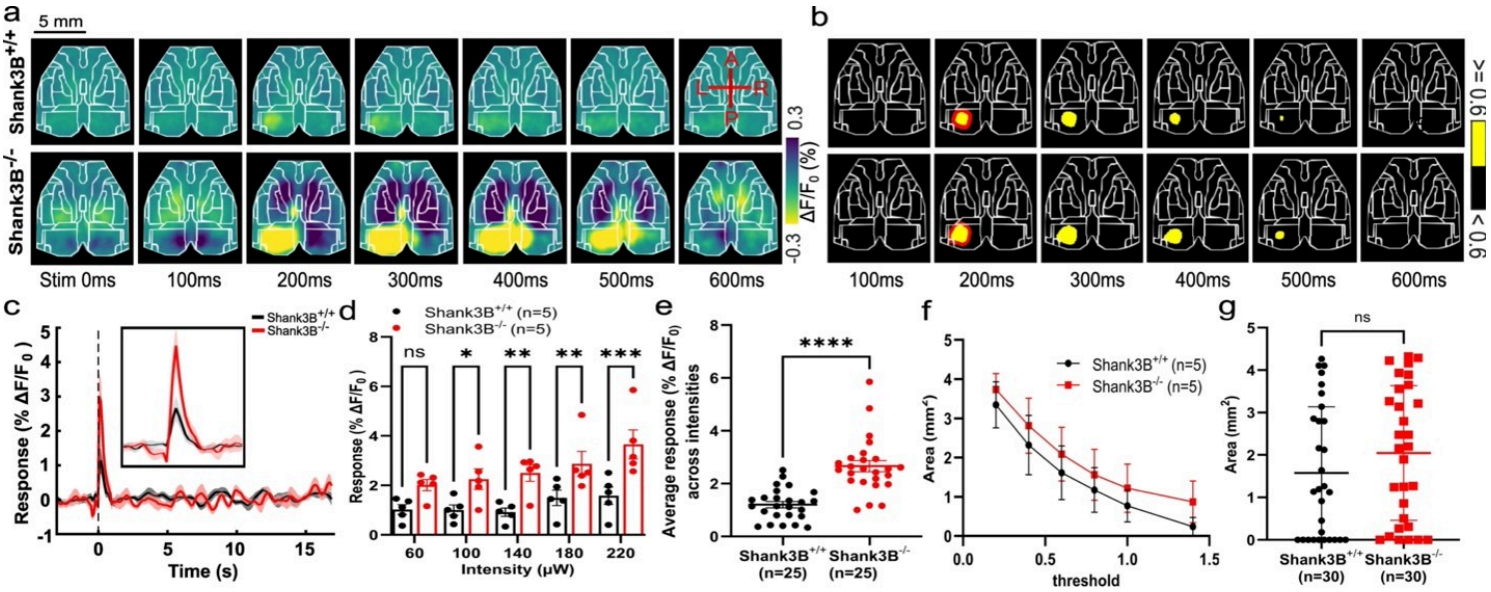

Figure 2

Shank3B$^{-/-}$ mice exhibit enhanced evoked responses and increased variability in visual cortex.
(a) Pseudocolor maps of $\Delta F/F_0$ showing visual-evoked activity in the dorsal cortex at 0, 100, 200, 300, 400, 500 and 600 ms post-stimulus for Shank3B$^{+/+}$ (top) and Shank3B$^{-/-}$ (bottom) mice. Color scale indicates $\Delta F/F_0$ amplitude.
(b) Time-resolved area of activation above an absolute $\Delta F/F_0$ threshold of 0.6 for visual stimuli at 100, 200, 300, 400, 500 and 600 ms post-stimulus for Shank3B$^{+/+}$ (top) and Shank3B$^{-/-}$ (bottom) mice. Color scale indicates below and above threshold.
(c) Mean $\Delta F/F_0$ time course (smoothed) in response to visual stimulation at the highest intensity.

Vertical line marks stimulus onset; inset shows a zoom-in on the peak response. Data are mean ± SEM across n = 5 mice.

(d) Peak $\Delta F/F_0$ amplitudes at five light intensities (60, 100, 140, 180, 220 μW) under visual stimulation for Shank3B$^{+/+}$ and Shank3B$^{-/-}$ mice. Data are mean ± SEM, n = 5 per group; *p<0.05, **p<0.01 (two-way ANOVA with Bonferroni's post-hoc).
(e) Average peak $\Delta F/F_0$ across all tested intensities (n = 25 (5 mice * 5 intensities)). ***p<0.0001 (t-test).
(f) Activated area as a function of $\Delta F/F_0$ threshold values under visual stimulation (n = 5 per group). *p<0.05 (two-way ANOVA).
(g) Mean activated area averaged across thresholds (same data as in f, n = 30 (5 mice * 6 threshold)). Data are mean ± SEM.

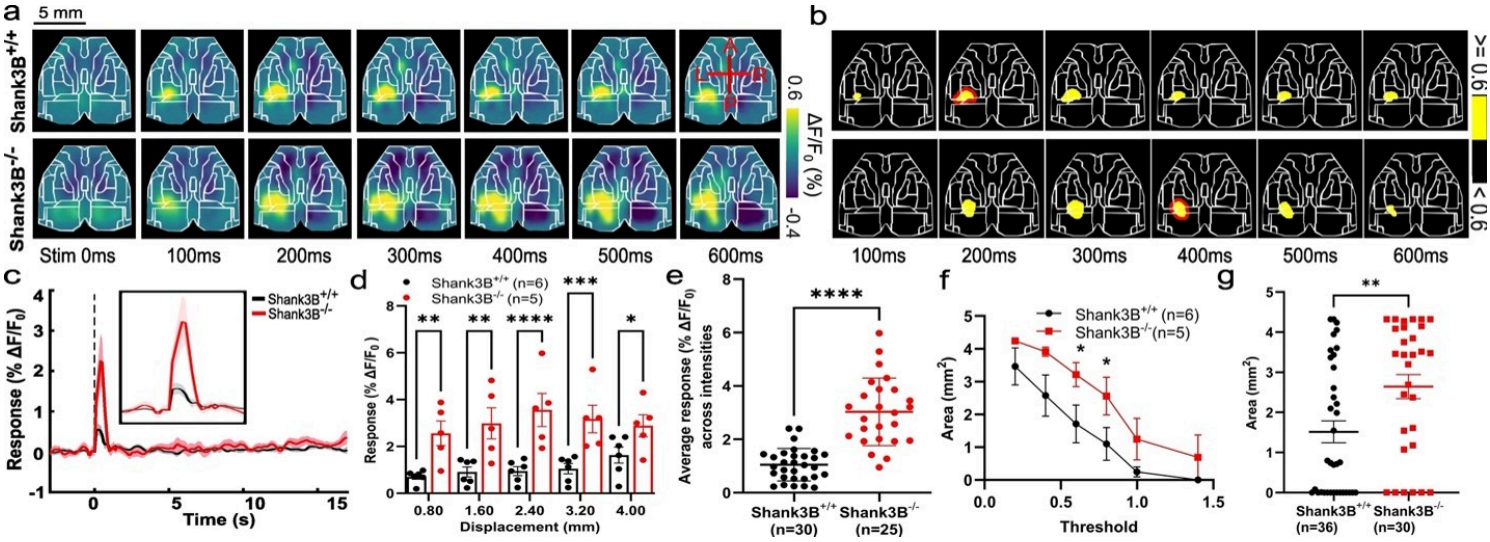

Figure 3

Shank3B$^{-/-}$ mice exhibit enhanced evoked responses and increased variability in somatosensory cortex.

(a) Pseudocolor maps of $\Delta F/F_0$ showing whisker-evoked activity in the dorsal cortex at 0, 100, 200, 300, 400, 500 and 600 ms post-stimulus for Shank3B$^{+/+}$ (top) and Shank3B$^{-/-}$ (bottom) mice. Color scale indicates $\Delta F/F_0$ amplitude.
(b) Time-resolved area of activation above an absolute $\Delta F/F_0$ threshold of 0.6 for whisker stimuli at 100, 200, 300, 400, 500 and 600 ms post-stimulus for Shank3B$^{+/+}$ (top) and Shank3B$^{-/-}$ (bottom) mice. Color scale indicates below and above threshold.
(c) Mean $\Delta F/F_0$ time course (smoothed) in response to whisker stimulation at the highest intensity. Vertical line marks stimulus onset; inset shows a zoom-in on the peak response. Data are mean ± SEM (Shank3B$^{+/+}$ n = 6, Shank3B$^{-/-}$ n = 5).
(d) Peak $\Delta F/F_0$ amplitudes at five whisker displacements (0.8, 1.6, 2.4, 3.2, 4.0 mm) under whisker stimulation for Shank3B$^{+/+}$ and Shank3B$^{-/-}$ mice. Data are mean ± SEM; *p<0.05, **p<0.01 (two-way ANOVA with Bonferroni's post-hoc). Same sample size as panel c.

(e) Average peak $\Delta F/F_0$ across all tested intensities (n = 25 or 30 (5 or 6 mice * 5 intensities). ***$p<0.0001$ (t-test).

(f) Activated area as a function of $\Delta F/F_0$ threshold values under whisker stimulation. *$p<0.05$ (two-way ANOVA). Same sample size as panel c.

(g) Mean activated area averaged across thresholds (same data as in h). Data are mean ± SEM. (n = 30 or 36 (5 or 6 mice * 6 threshold).

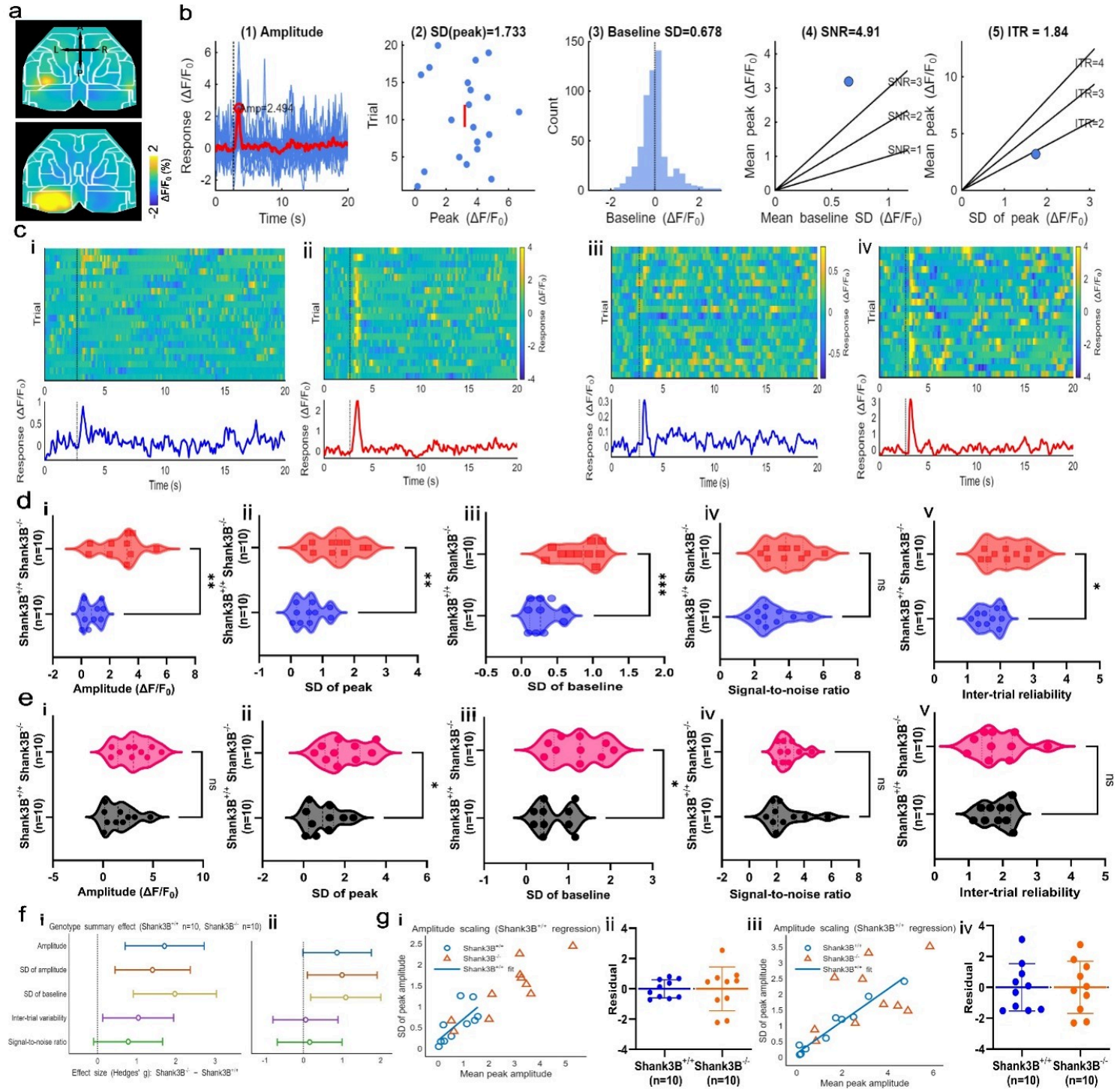

Figure 4

Sensory-evoked response amplitude, variability, and scaling under whisker and visual stimulation in Shank3B mice.

(a) Representative wide-field mesoscale calcium imaging maps showing stimulus-evoked cortical responses. Left, response amplitude map during whisker stimulation; right, response amplitude map during visual stimulation. **(b)** Illustration of five evoked-response metrics derived from a representative cortical ROI. Panel 1 shows individual trial time courses (blue) overlaid with the trial-averaged response (red). Panel 2 depicts the distribution of peak response amplitudes across trials, with variability summarized as the SD of peak amplitude. Panel 3 shows the distribution of baseline activity, quantified as the SD of baseline activity. Panel 4 illustrates the relationship between baseline variability and mean peak response amplitude, from which the signal-to-noise ratio (SNR) is derived. Panel 5 shows the relationship between peak response amplitude and trial reliability, from which inter-trial reliability (ITR) is computed.

(c) Trial-by-trial response heatmaps and corresponding time courses illustrate variability in evoked activity across trials for representative animals. Panels i and ii show whisker stimulation, while panels iii and iv show visual stimulation. Panels i and iii are from $Shank3B^{+/+}$ mice, and panels ii and iv are from $Shank3B^{-/-}$ mice. **(d)**Distribution of whisker-evoked response metrics across animals for $Shank3B^{+/+}$ (blue) and $Shank3B^{-/-}$ (red) mice. Metrics include peak response amplitude, SD of peak amplitude, SD of baseline, signal-to-noise ratio, and inter-trial variability. Each dot represents one animal; violin plots illustrate group-level distributions. **(e)** Same response metrics shown for visual stimulation. **(f)** Genotype summary effects for all response metrics, expressed as Hedges' g with 95% confidence intervals. Positive values indicate larger metric values in $Shank3B^{-/-}$ mice relative to $Shank3B^{+/+}$ mice. Left, whisker stimulation; right, visual stimulation. Error bars denote confidence intervals; each line corresponds to one metric. **(g)** Amplitude scaling analysis. (i, iii) Relationship between mean peak response amplitude and SD of peak amplitude for individual animals (i, whisker stimulation; iii, visual stimulation). $Shank3B^{+/+}$ animals (blue circles) define a linear amplitud-variability scaling relationship (solid blue line), while $Shank3B^{-/-}$ animals (red triangles) are overlaid for comparison. Regression lines are fit only to $Shank3B^{+/+}$ data. (ii, iv) Residuals relative to the $Shank3B^{+/+}$-defined scaling relationship (ii, whisker stimulation; iv, visual stimulation), plotted by genotype ($Shank3B^{+/+}$, blue; $Shank3B^{-/-}$, orange).

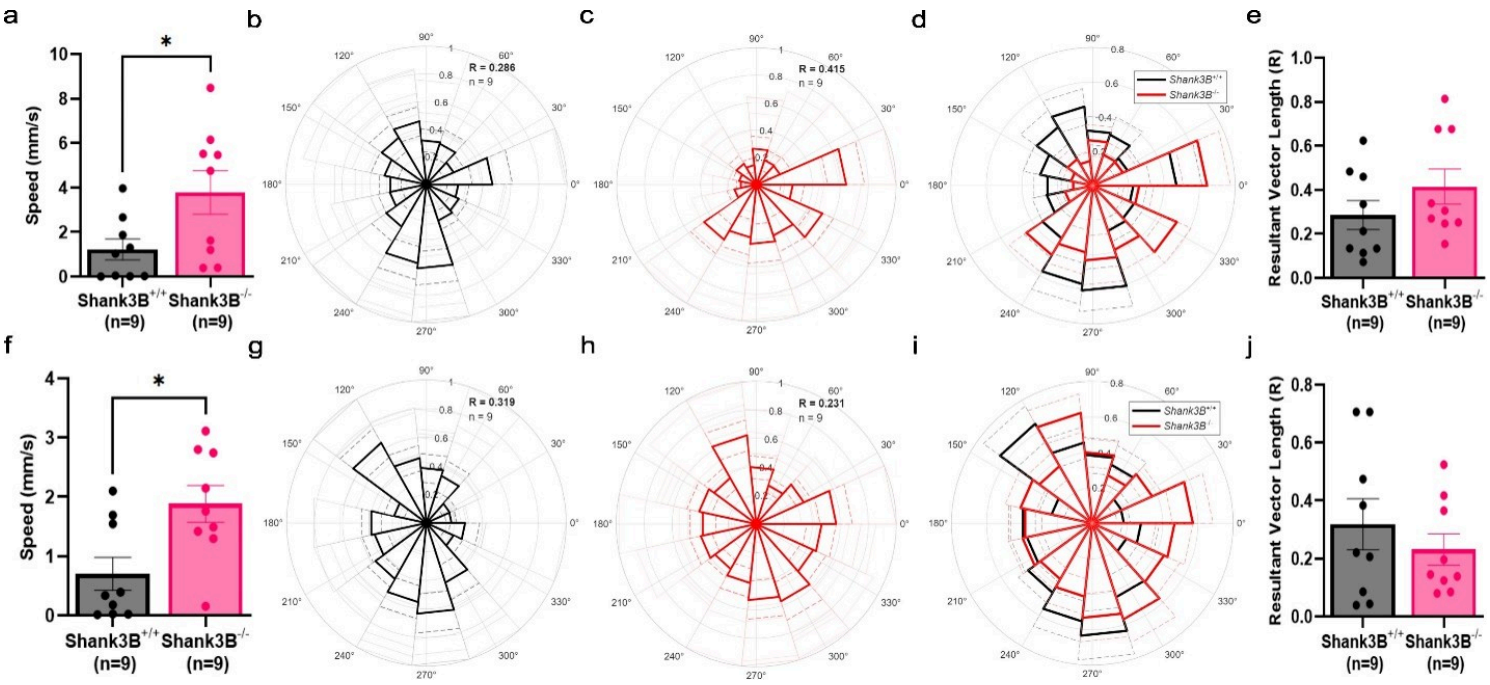

Figure 5

Faster propagation speed and preserved direction in Shank3B$^{-/-}$ mice during both visual and whisker stimulation.

(a) Mean propagation speed (mm/s) for visual stimulation. Bars show group mean ± SEM; dots represent individual animals. Shank3B$^{-/-}$ mice showed significantly faster propagation. (b,c) Polar histograms of instantaneous flow direction for visual stimulation: (b) Shank3B$^{+/+}$, (c) Shank3B$^{-/-}$. Thick lines show group mean; dashed lines show mean ± SEM. Directions were binned into 15 bins of 24°. Anatomical convention: 0° = medial, 90° = anterior, 180° = lateral, 270° = posterior. Radial axis shows max-normalized bin counts. (d) Overlay of Shank3B$^{+/+}$ (black) and Shank3B$^{-/-}$ (red) direction histograms for visual stimulation. (e) Resultant vector length (R) for visual stimulation. No significant genotype difference. (f) Mean propagation speed (mm/s) for whisker stimulation. Shank3B$^{-/-}$ mice showed significantly faster propagation. (g,h) Polar histograms of instantaneous flow direction for whisker stimulation: (g) Shank3B$^{+/+}$, (h) Shank3B$^{-/-}$. Format as in (b,c). (i) Overlay of direction histograms for whisker stimulation. (j) Resultant vector length (R) for whisker stimulation. No significant genotype difference. n = 9 per group throughout.

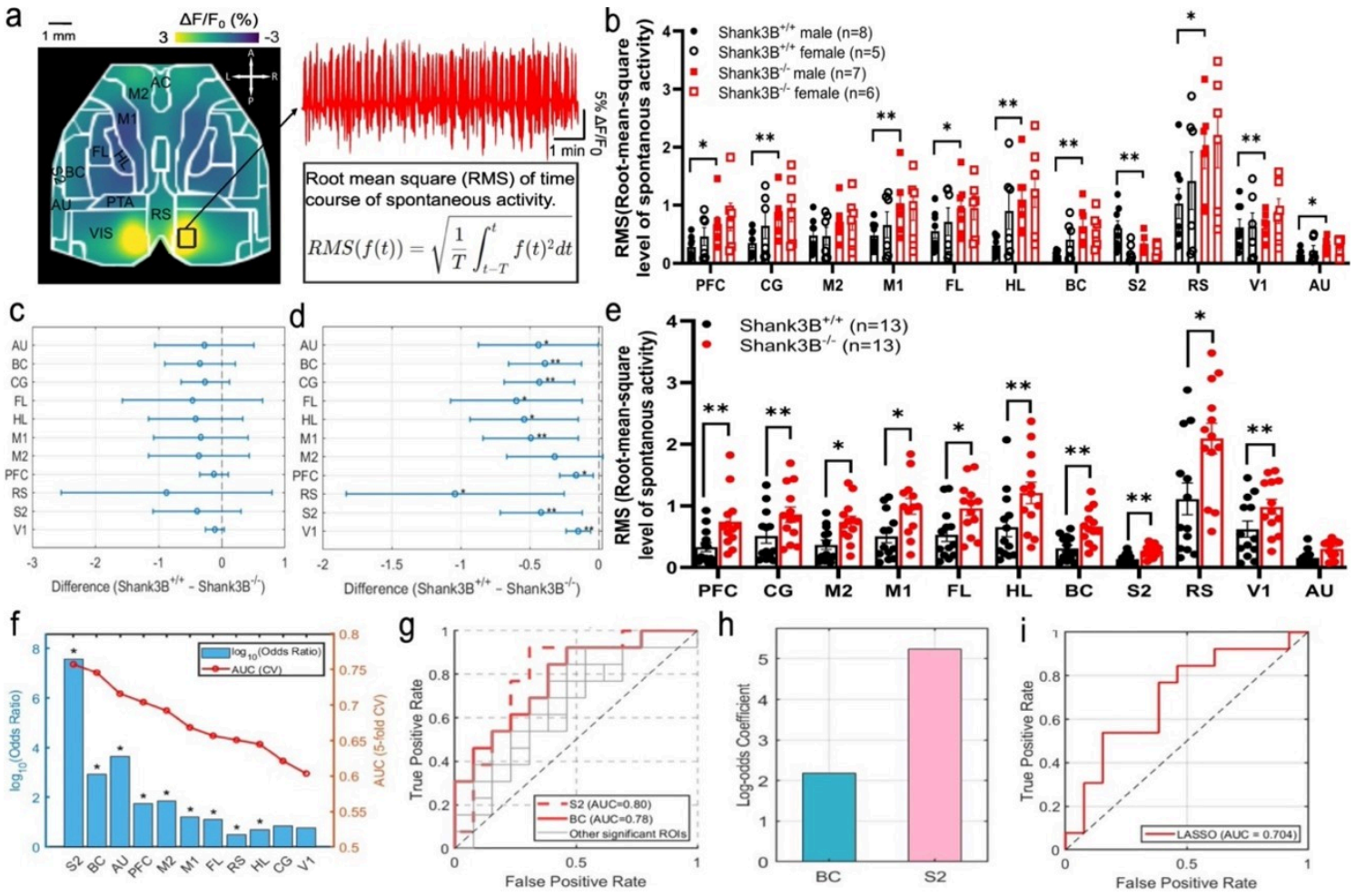

Figure 6

Shank3B$^{-/-}$ mice exhibit widespread increases in spontaneous cortical activity, with strongest genotype separation in somatosensory regions.

(a) Schematic of cortical regions in the imaging field of view. Left: The map of resting $\Delta F/F_0$ over the dorsal cortex with ROI boundaries (PFC, prefrontal cortex; CG, cingulate cortex; M2, the secondary motor cortex; M1, the primary motor cortex; FL, the forelimb somatosensory cortex; HL, the hindlimb somatosensory cortex; BC, barrel cortex; S2, the secondary somatosensory cortex; RS, retrosplenial cortex; V1, the primary visual cortex; AU, auditory cortex); scale bar = 1 mm. **Right, example $\Delta F/F_0$ trace from one ROI, and definition of RMS used to quantify spontaneous activity.**

(b) RMS of spontaneous activity in 11 cortical ROIs, plotted by genotype and sex (Shank3B$^{+/+}$ male n = 8, female n = 5; Shank3B$^{-/-}$ male n = 7, female n = 6).

(c, d) Genotype differences in RMS for each ROI (Shank3B$^{+/+}$ - Shank3B$^{-/-}$), shown separately for females (c) and males (d). Error bars indicate 95% confidence intervals based on post hoc comparisons from two-way ANOVA.

(e) RMS of spontaneous activity pooled across sex (n = 13 per genotype).

(f) Summary of univariate logistic regression results using RMS in each ROI to classify genotype. Blue bars show $\log_{10}$-transformed odds ratios; red line shows cross-validated AUC (5-fold).

(g) ROC curves for S2 and BC, the two ROIs with highest predictive performance.

(h) Coefficients from multivariate LASSO logistic regression; only S2 and BC retained non-zero weights.

(i) ROC curve for full LASSO model.

Bars represent mean ± SEM. Statistical comparisons in (b, e) used two-way ANOVA (with sex as a factor) and unpaired t-tests, respectively; post hoc tests used Bonferroni correction. In (f), p-values refer to likelihood-ratio test results comparing each model to a null model. *p < 0.05, **p < 0.01.

Supplementary Files

This is a list of supplementary files associated with this preprint. Click to download.

- Supplementaryinformation.docx